Electrochimica Acta 150 (2014) 232–244

Contents lists available at ScienceDirect

Electrochimica Acta

journal homepage: www.elsevier.com/locate/electacta

Multi-scale Modelling of Electrochemically Promoted Systems

Ioannis S. Fragkopoulos, Constantinos Theodoropoulos *

School of Chemical Engineering and Analytical Science, University of Manchester, Manchester M13 9PL, UK

ARTICLE INFO

Article history:
Received 27 June 2014
Received in revised form 21 October 2014
Accepted 21 October 2014
Available online 29 October 2014

Keywords:
NEMCA
backspillover
multi-scale modelling
CFD-kMC coupling
Electrochemically Promoted CO oxidation on Pt/YSZ

ABSTRACT

The objective of this work is the formulation of a multi-scale framework for electrochemically promoted systems. We have constructed a 3-Dimensional, isothermal, solid oxide single pellet, multi-scale framework, which describes the chemical and electrochemical phenomena taking place in a solid oxide single pellet under closed-circuit conditions, while the electrochemically promoted oxidation of CO over Pt/YSZ is used as an illustrative system. The proposed framework combines a 3-D macroscopic model which employs the finite element method (FEM) for the simulation of the charge transport and the electrochemical phenomena taking place in the pellet, and an in-house developed efficient implementation of a 2-D lattice kinetic Monte Carlo method (kMC) for the simulation of the reaction-diffusion micro-processes taking place on the catalytic surface. Comparison between the multi-scale framework and a macroscopic model [1] is carried out for several sets of operating conditions. Differences between the steady-state outputs of the two models are presented and discussed. A subsequent parametric study using the multi-scale framework is performed to investigate the effect of the gaseous species partial pressures and of the temperature on the CO_2 production rate.

1. Introduction

This work focuses on the development of a multi-scale framework for accurate simulations of electrochemically promoted systems. The electrochemical promotion of catalysis (EPOC) phenomenon accounts for the alteration of the activity of a catalyst, with a subsequent catalytic performance enhancement, of a metal (or metal oxide) deposited on a solid electrolyte, by means of electrical polarisation [2]. The addressed phenomenon, also referred to as non-Faradaid electrochemical modification of catalytic activity (NEMCA), was for the first time reported in the early 1980s by Vayenas and co-workers [3] and has since been investigated extensively by several research groups all around the world.

The reduction of environmental pollution has become an issue of great concern, requiring more sustainable and more efficient methods of exhaust emissions conversion. Air pollutants, such as carbon monoxide, nitrogen oxides, hydrocarbons and organic emissions, are very effectively being converted to harmless emissions, using appropriate cost-effective heterogeneous catalytic systems. Nevertheless, the use of heterogeneous catalysis bears some significant bottlenecks, such as the short catalytic life time due to deactivation, the high system preparation cost since most of the catalytic systems comprise of pricy metals (e.g. Pt) and the incapability of controlling the catalytic performance 'in situ' [4].

The EPOC phenomenon is a promising candidate revealing a great potential in the gaseous emissions treatment technology, since it can increase the life time of the catalyst as well as its activity, leading to lower catalyst loading and to subsequent lower operating costs, modify the selectivity to the desired products and control the catalytic performance during an electrocatalytic process [4,5].

The main objective of this work is the development of an accurate multi-scale framework to describe the effect of electrochemical promotion and to obtain insights for the chemical micro-processes taking place on the catalytic film under closed-circuit conditions.

In a recent study [1], we have developed a multi-dimensional macroscopic model to describe the chemical and electrochemical processes taking place in an electrochemically promoted CO combustion system and to quantify the non-Faradaic catalytic performance enhancement upon polarisation. The proposed model was utilised in conjunction with literature data for the estimation of parameters that are of great importance for EPOC system simulations. Sensitivity analysis for the estimated parameters was

---

Abbreviations: BSS, backspillover species; CFD, computational fluid dynamics; CTMC, continuous time Monte Carlo; EPOC, electrochemical promotion of catalysis; FEM, finite elements method; kMC, kinetic Monte Carlo; NEMCA, non-Faradaic electrochemical modification of catalytic activity; SOFC, solid oxide fuel cell; TPB, triple phase boundary; YSZ, yttria-stabilized zirconia.

* Corresponding author. Tel.: +44 (0) 161 306 4386; fax: +44 (0) 161 236 7439.
E-mail address: k.theodoropoulos@manchester.ac.uk (C. Theodoropoulos).

http://dx.doi.org/10.1016/j.electacta.2014.10.100

Nomenclature

E_A	activation energy of a reaction, J mol^{-1}
F	Faraday constant, A s mol^{-1}
$I^{A/C}$	current density distribution of anode/cathode, A m^{-2}
I_0	exchange current density, A m^{-2}
k_{diff}	diffusion micro-process rate constant, s^{-1}
k_i^a	adsorption rate constant of micro-process i, s^{-1}
k_i^d	desorption rate constant of micro-process i, s^{-1}
k_i^r	surface reaction rate constant of micro-process i, s^{-1}
$k_{o,i}$	pre-exponential coefficient of micro-process i, s^{-1}
N_{AV}	Avogadro constant, mol^{-1}
n_r	total number of micro-processes
N_s	concentration of active sites on catalytic surface, mol m^{-2}
M_j	molecular weight of species *j*, kg mol^{-1}
P_{A^*}	one site conditional probability
P_{A^*/B^*}	two site conditional probability
P_i	partial pressure of species *i*, atm
P_T	system operating (reference) pressure, atm
Q_i	charge source term of medium i, A m^{-3}
R	ideal gas constant, J mol^{-1} K^{-1}
$\hat{R}_i$	overall rate of species i, mol s^{-1}
S_j	sticking coefficient of species *j*
T_s	temperature at the catalytic surface, K
T	absolute temperature, K
t	time, s
V_{OC}	Nernst potential, *V*
X_j	mole fraction of species *j*

Greek symbols

α	charge transfer coefficient
$\hat{\Gamma}_i$	transition probability of micro-process *i*, s^{-1}
$\hat{\Gamma}_T$	total transition probability, s^{-1}
η	overpotential, *V*
μ_i	chemical potential of species *i*, J mol^{-1}
π	mathematical constant
ρ_i	charge density of medium *i*, A m^{-3}
σ_i	charge conductivity of medium *i*, Ω^{-1} m^{-1}
Φ_i	local electrostatic potential of medium *i*, *V*
Φ_{op}	operating potential in the solid oxide single pellet, *V*
Ω_{A^*}	size of class A^*
Ω_T	total number of lattice sites

Superscripts and subscripts

A	anode
Au	gold
C	cathode
CO	carbon monoxide
CO_2	carbon dioxide
el	electronic
g	gas phase
io	ionic
O	oxygen
O^{2-}	oxygen anion
$[O^{\delta-}\text{-}\ \delta+]$	backspillover species
o	standard conditions
Pt	platinum

carried out to quantify the effect of each parameter on the CO_2 production rate. We found that varying the electrochemical kinetic parameters has practically no impact on the predicted CO_2 production rate, while altering the chemical ones can lead to vast changes of the obtained CO_2 production rate. It was also established that the dominant effect in such a system is non-Faradaic.

The NEMCA and Faradaic contributions to the system are taking place at different length-scales. The NEMCA effect is limited to the catalyst surface (whose size is on the order of nm), while the Faradaic effect depends on the volume of the entire system (order of μm). Hence, in this study we have extended the work in Fragkopoulos et al. [1] to the formulation of a multi-scale framework to investigate the NEMCA (catalytic processes) and Faradaic (charge transport and triple phase boundary (TPB) electrochemical processes) phenomena taking place in the system at their appropriate length-scales.

Physical phenomena taken into consideration in engineering systems are by nature occuring at different length- and time-scales with varying degrees of complexity. Multi-scale modelling accounts for the construction of a composite mathematical framework that links two or more computational models describing such diverse and complex phenomena [6]. Fig. 1 illustrates a relation between various levels of length- and time-scales with macro-, meso- and micro-scale computational approaches. The macro-scale approach corresponds to the entire flow domain (continuum methods), the micro-scale approach to the molecular level (molecular dynamics, density function theory) and the meso-scale approach to the level between the macro- and micro-scale ones (meso-mechanics).

Communication between the different scales (multi-scale modelling) can be attained through the use of hierarchical or hybrid (concurrent) methods [7]. In the hierarchical method, the simulation of the physical phenomena begins at a smaller scale and the calculated properties are delivered to a larger level, while the hybrid method accounts for more complex simulations where three (or more) different methods are interacting. Furthermore, the classification of multi-scale models also relies on the technique that the submodels are coupled [8,9,10]. A multi-scale approach can consequently be considered as multi-domain, embedded, parallel, serial and simultaneous [8].

The multi-scale approach is very promising nowadays in the field of electrochemistry and especially in solid oxide fuel cell (SOFC) systems, where state-of-the-art frameworks [11–14] have been developed to link the transport phenomena taking place at the macro-scale, with electrochemical reactions and material properties accurately described at the meso- and micro-scales. Khaleel et al. [12] presented a multi-scale approach where the microscopic model employs the Lattice-Boltzmann method to investigate the performance of a porous electrode, calculating the

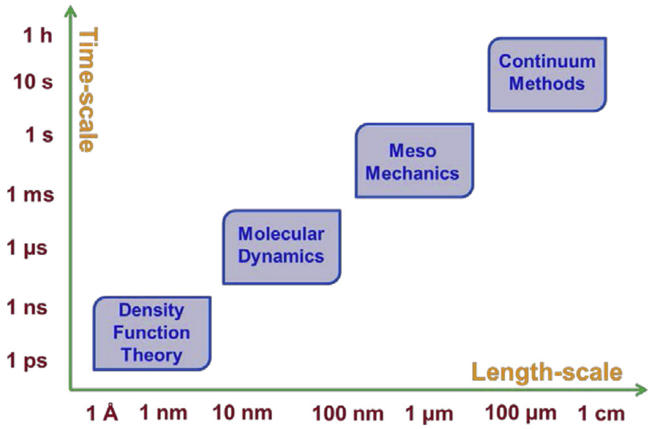

Fig. 1. Characteristic length- and time-scales for various modelling methods.

overall SOFC current-voltage relation and taking into consideration the structure of the electrode at the micro-structure scale, transportation of oxygen ions as well as reaction surfaces distribution. The evaluated current-voltage relation is subsequently fed to the macroscopic model which performs cell voltage, current density and heat production calculations employing the FEM. Bessler et al. [11] performed multi-scale simulations to describe transport in an internal-reforming SOFC operated on CH_4/H_2O mixtures. The framework is integrated by a macroscopic model, which is used for simulating the transport of the gas-phase in the SOFC channel, the charge transport as well as continuum mass in the porous electrodes, and a microscopic model which is employed for the simulation of mass transport over the TPBs. Kim et al. [13] formulated a multi-scale framework to predict the performance of a SOFC when micro-structure evolution takes place at the anode. In that study, the framework integrates a macroscopic model which simulates the charge and mass transport as well as the electrochemical phenomena, and local material properties such as triple phase boundary density, electrical conductivity and gas diffusivity are calculated through evolving the micro-structure. Lee and Hong [14] developed a multi-scale technique for the design of a novel intermediate-temperature planar-type micro SOFC stack system. The proposed multi-scale approach, couples a computational fluid dynamics (CFD) model which is employed for the simulation of the fuel and air flows, with molecular dynamics simulations which are employed for determining the optimal composition of an electrolyte used in intermediate temperature simulations.

Despite the increasing use of multi-scale frameworks in SOFC systems, such a modelling approach has not been formulated yet for the simulation of electrochemically promoted systems.

In this work, we have constructed a multi-scale framework to describe the effect of electrochemical promotion in a solid oxide single pellet system. The proposed framework links a 3-D macroscopic model used to perform charge transport simulations throughout the solid oxide single pellet employing CFD software (COMSOL Multiphysics), with a 2-D microscopic model used to simulate the reaction-diffusion processes taking place at the anode working electrode (catalytic surface) employing the lattice kinetic Monte Carlo method. Similar to the study presented in Fragkopoulos et al. [1], the electrochemically promoted CO oxidation over Pt/YSZ is chosen as an illustrative scheme. To examine the added value of such a multi-scale model, comparisons between the proposed framework and the macroscopic model [1] dynamic and steady state outputs are performed for various sets of operating conditions. Subsequent parametric investigation using the multi-scale framework is carried out to analyse the effects of the partial pressure and of the temperature on the CO_2 production rate and finally, outcomes from the above study are discussed.

2. Electrochemically promoted multi-scale CO combustion

The electrochemically promoted multi-scale CO combustion over Pt/YSZ is here the system of interest [1]. The reactor utilised in the proposed framework is considered as well mixed and it is of single-pellet type meaning that the entire pellet is exposed to the reacting gas mixture. The reactor design and the 3D computational domain of the single pellet are illustrated in Fig. 2, where Yttria Stabilized Zirconia (YSZ) is utilised as electrolyte, while Pt and Au are used as anode and cathode electrodes respectively. The physical dimensions of the single pellet are tabulated in Table I and it should be noted that both Pt and Au electrodes are considered as 2-dimensional (i.e. negligible thickness) layers on YSZ.

The proposed multi-scale framework integrates the reaction-diffusion phenomena, taking place on the catalytic surface (Pt), the charge transport throughout the pellet, as well as the electrochemical processes taking place at the triple phase boundaries. The catalytic surface processes for this system are represented in Fig. 3, while the mechanisms of the chemical (CO oxidation reaction mechanism as proposed by Kaul et al. [15] augmented by reactions (4)–(6) involving the backspillover species (BSS) due to the circuit closure) and of the electrochemical processes taken into consideration in this study are tabulated in Tables II and III respectively.

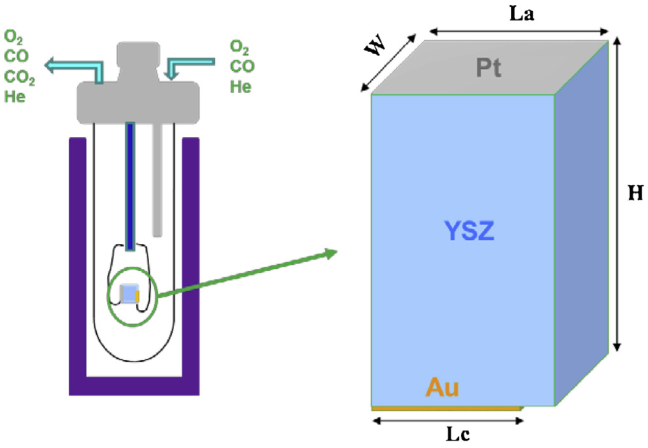

Fig. 2. Reactor design and 3-D computational domain.

COMSOL Multiphysics [16], is employed for the simulation of the charge conservation in the pellet at the macroscopic level, while an in-house developed lattice kinetic Monte Carlo model [17–19] is utilised for the simulation of the reaction-diffusion micro-processes taking place on the catalytic surface at the microscopic level. The proposed framework can be used to obtain electronic and ionic potential curves throughout the pellet as well as species' coverage profiles at the micro-catalytic surface. It can also provide the transient behaviour of the gas mixture concentration in the reactor and of the CO_2 production rate.

2.1. Model assumptions

The main assumptions that have been made for this 3-D multi-scale framework are listed below:

- The gas phase pressure in the reactor as well as the temperature on the catalytic surface and throughout the reactor are considered constant.
- The gaseous mixture in the reactor is considered to be well mixed and to behave as an ideal gas.
- The framework accounts only for the catalytic micro-processes on Pt while the catalytic effect of Au (in presence of Pt), can be neglected [20].
- Only the diffusion micro-process of BSS is taken into account as a simplification to the mass transport on the Pt, since for the other species the dominant micro-processes are the adsorption and desorption ones.

Table I
The physical dimensions of the solid oxide single pellet.

Parameter	Symbol	Value
Electrolyte/Anode length, m	L_a	460×10^{-9}
Cathode length, m	L_c	400×10^{-9}
Electrolyte/Anode/Cathode width, m	W	102.3×10^{-9}
Electrolyte height, m	H	5×10^{-6}

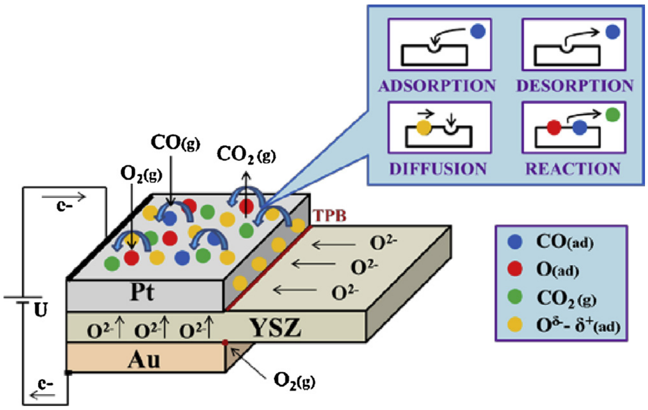

Fig. 3. Schematic presentation of the electro-catalytic surface dynamics.

- Assuming that both electrolyte and electrodes are good charge conductors, the operating potential difference throughout the pellet is considered to be constant.
- The electrodes of the cathode and the anode are modelled as ‘flat’ (2-D) surfaces deposited on the electrolyte domain.
- The electrochemical reactions are considered to take place only at the anodic and cathodic TPBs, represented here by the edges of the respective electrodes.
- The chemical potential of BSS is assumed to be equal with the one of the O^{2-} on the surface of YSZ ($\mu_{BSS} = \mu_{O^{2-}_{YSZ}}$) [1].

2.2. The microscopic model

The microscopic model used here, employs a stochastic methodology for the simulation of the catalytic surface dynamics. Gillespie [21,22] was one of the first authors to use a stochastic approach for simulations of simple homogeneous reacting systems. This probabilistic approach (an extension of the well-known Monte Carlo method proposed by Metropolis and Ulam [23] has since been extensively improved and employed for complex heterogeneously catalysed reaction system kinetic simulations, where the catalytic surface is either represented by a lattice taking into account the spatial distribution and the local micro-kinetics [24,25] or not taking into consideration any spatial representation [26–28]. In the cases where the catalytic surface is represented by a lattice, this method is referred to as the lattice kinetic Monte Carlo.

Table II
The scheme of catalytic surface micro-processes.

Open-circuit CO oxidation micro-processes		
Adsorption/desorption of O_2	$O_{2(g)} + 2* \underset{k^d_{-1}}{\overset{k^a_1}{\rightleftarrows}} 2O*$	(1)
Adsorption/desorption of CO	$CO_{(g)} + * \underset{k^d_{-2}}{\overset{k^a_2}{\rightleftarrows}} CO*$	(2)
Surface reaction between adsorbed CO and O	$O * + CO * \overset{k^r_3}{\rightarrow} CO_{2(g)} + 2*$	(3)
Closed-circuit additional micro-processes		
Surface reaction between adsorbed CO and BSS	$BSS * + CO * \overset{k^r_4}{\rightarrow} CO_{2(g)} + 2*$	(4)
Desorption of BSS	$2BSS * \overset{k^d_5}{\rightarrow} O_{2(g)} + 2*$	(5)
BSS Surface diffusion	$BSS * + * \overset{k^{BSS*}_{diff}}{\rightarrow} * + BSS*$	(6)

Table III
The scheme of electrochemical reactions.

Cathodic TPB:	$3 \times \left[\frac{1}{2}O_{2(g)} + 2e^- \rightarrow O^{2-}_{YSZ}\right]$(7)
Anodic TPB:	$O^{2-}_{YSZ} + CO_{(g)} \rightarrow CO_{2(g)} + 2e^-$(8) $O^{2-}_{YSZ} \rightarrow \frac{1}{2}O_{2(g)} + 2e^-$(9) $O^{2-}_{YSZ} \rightarrow BSS + 2e^-$(10)

The kinetic Monte Carlo method is used to perform stochastic simulations for the probabilistic master equation [29]:

$$\frac{\partial P_{n,t}}{\partial t} = \sum_m [W_{m\rightarrow n}P_{m,t} - W_{n\rightarrow m}P_{n,t}] \tag{11}$$

where n and m are successive configurations of the catalytic surface, $P_{n,t}$ is the probability that the lattice is in configuration n at time t, and $W_{màn}$ is the probability per unit time that the lattice will undergo a transition from configuration m to configuration n. Due to the large number of possible configurations, the solution of the master equation (11) cannot be achieved analytically for real system simulations. For this reason, Monte Carlo algorithms are often employed to perform the computational intensive simulations efficiently.

In this work, we have employed an in-house developed lattice kMC model based on the continuous time Monte Carlo (CTMC) algorithm proposed by Reese et al. [24], for the simulation of the reaction-diffusion micro-processes taking place on the catalytic lattice. The main features of the CTMC algorithm exploited here are summarised in the following 5 steps:

1. *Initialisation of the lattice.* The surface species, i.e. O*, CO*, BSS*, are randomly positioned on the micro-lattice according to the given initial respective number of molecules.
2. *Creation of classes* (*i.e.* combinations (or pairs) of reactive surface species). After distributing the species on the catalytic lattice, classes (of species) are formed and the size of each class is computed. The size (total number) of each class is used in the calculation of conditional probabilities (see Eq.(20)). The conditional probabilities necessary for obtaining the micro-processes rates (termed as transition probabilities) are described below (Eq.(14) to Eq.(19)).
3. *Selection of a micro-process.* The probabilistic selection of the micro-process to occur in the current time interval takes place through the following inequality:

$$\sum \hat{\Gamma}_{i_{i=1}}^{k-1} < R_1 \hat{\Gamma}_i < \sum_{i=1}^{k} \hat{\Gamma}_i, \text{with } R_1 \in (0,1) \text{ and } (1 < k < n_r) \tag{12}$$

where R_1 is a random number, $\hat{\Gamma}_i$ is the transition probability of micro-process i, n_r is the total number of micro-processes, and $\hat{\Gamma}_T$ the total transition probability whichis expressed as the sum of the individual transition probabilities:

$$\hat{\Gamma}_T = \sum_{i=1}^{n_r} \hat{\Gamma}_T \tag{13}$$

The transition probability for each micro-process i (as in Table II) is given by:

$$\hat{\Gamma}_1 = k^a_1 P_* P_{*/*} \text{ and } \hat{\Gamma}_{-1} = k^d_{-1} P_{O^*} P_{O^*/O^*} \tag{14}$$

$$\hat{\Gamma}_2 = k^a_2 P_* \text{ and } \hat{\Gamma}_{-2} = k^d_{-2} P_{CO^*} \tag{15}$$

$$\hat{\Gamma}_3 = k_3^r (P_{O^*} P_{CO^*/O^*} + P_{CO^*} P_{O^*/CO^*}) \tag{16}$$

$$\hat{\Gamma}_4 = k_4^r (P_{BSS^*} P_{CO^*/BSS^*} + P_{CO^*} P_{BSS^*/CO^*}) \tag{17}$$

$$\hat{\Gamma}_5 = k_5^d P_{BSS^*} P_{BSS^*/BSS^*} \tag{18}$$

$$\hat{\Gamma}_{diff} = k_{diff}^{BSS} (P_{BSS^*} P_{*/BSS^*} + P_* P_{BSS^*/*}) \tag{19}$$

where k_i^a, k_i^d and k_i^r are the adsorption, desorption and surface reaction rate constants respectively, k_{diff} is the diffusion micro-process rate constant, P_{A^*} and P_{A^*/B^*} are the one and two site conditional probabilities, respectively.The one site conditional probability, P_{A^*}, expresses the probability of selecting a site occupied by A*, while the two site one, P_{A^*/B^*}, expresses the probability of picking a site occupied by B* after choosing an adjacent site occupied by A*. The conditional probabilities P_{A^*} and P_{A^*/B^*} are given by [24]:

$$P_{A^*} = \frac{\Omega_{A^*}}{\Omega_T} \quad \text{and}\, P_{A^*/B^*} = \frac{\sum_{j=1}^{4} j \cdot (\Omega_{B^*A^*j})}{4 \cdot \Omega_{B^*}} \tag{20}$$

where Ω_{A^*} is the number of sites occupied by A*, Ω_T is the total number of lattice sites, $\Omega_{B^*A^*j}$ is the number of sites of identity B* that have j adjacent sites of identity A* (also referred to as size of class B*,A*,j). Number 4 in the denominator of Eq.(20) is the maximum number of the adjacent sites that a selected site can have (the diagonally adjacent sites are not taken into account in this scheme).The individual adsorption rate constants, k_i^a, are expressed using the gas collision theory as [25,30]:

$$k_i^a = \frac{S_j P_T X_j}{N_s} \left(\frac{1}{2\pi M_j R T_s}\right)^{1/2} \quad i = 1 (j = O_2) \ \text{and} \ \ i = 2 (j = CO) \tag{21}$$

where S_j is the sticking coefficient of gaseous species j, P_T is the system operating pressure, X_j is the mole fraction of gas species j, N_s is the concentration of active sites on the catalytic surface, M_j is the molecular weight of species j and T_s is the temperature of the catalytic surface.The individual desorption, k_i^d, and surface reaction, k_i^r, rate constants follow the Arrhenius expression:

$$k_i^{d,r} = k_{o,i}^{d,r} \exp\left(\frac{-E_{A,i}^{d,r}}{RT_S}\right), \quad i = -1, -2, 3 \tag{22}$$

where $k_{o,i}$ and $E_{A,i}$ are the pre-exponential factor and the activation energy for each micro-process i, respectively.The diffusion micro-process rate constant, k_{diff}, can be related with the continuum diffusion coefficient, D_i, using a similar correlation to the one presented in Phillips [31] and in Tello and Curtin [32]:

$$k_{diff} = D_i \frac{1}{A_S} = D_i \frac{N_S N_{AV}}{\Omega_T} \tag{23}$$

where N_{AV} is the Avogadro constant, N_S is the catalyst site density, Ω_T is the total number of lattice sites and A_S is the catalyst surface area.

4. *Selection of lattice sites and reaction.* Having found probabilistically (using Eq.(12)) which micro-process is to occur, we randomly select a class associated with the chosen micro-process. Consequently, lattice sites that belong to the selected class are randomly picked and the micro-process takes place. Finally, an update of the number of surface and gaseous species, of the size of classes and subsequently of the conditional and of the transitional probabilities follows.
5. *Update of time variable.* After the chosen micro-process takes place, the time interval, $\Delta t_{\text{micro-process}}$, for this kMC event is calculated using a random number R_2 [22,30]:

   $$\Delta t_{micro-process} = \ln\left(\frac{1}{R_2}\right) \frac{1}{\Omega_{\hat{\Gamma}_T}}, \text{with}\, R_2 \in (0, 1) \tag{24}$$

   The simulation time is then updated using the following expression:

   $$t_j = t_{j-1} + \Delta t_{micro-process} \tag{25}$$

   where t_{j-1} is the value for the time before each micro-process takes place and t_j is the updated value for the time (after each micro-process takes place).

After updating the time variable, we start again from step 3 (selection of micro-process) and we follow the same process. This iterative process is continued until the given time reporting horizon, t_{rep}^{kMC}, is reached.

The rates of consumtion/production of the gaseous phase species due to the catalytic micro-processes taken into consideration in the kMC algorithm are given by:

$$\hat{R}_i^{KMC} = \frac{molecules\, of\, i}{N_{AV} t_{rep}^{kMC}} \tag{26}$$

where N_{AV} is the Avogadro constant, t_{rep}^{kMC} is the time reporting horizon used for every kMC run and *molecules of i* is the number of molecules of species i produced (positive sign) or consumed (negative sign) within the kMC time reporting horizon.

2.3. The macroscopic model

The macroscopic model utilised here consists of a set of PDEs to describe the charge conservation in the solid oxide single pellet. The charge transport in a non-porous media *i*, is described by the Poisson equation as follows [1,33]:

$$\frac{d\rho_i}{dt} = -\nabla(-\sigma_i \nabla \Phi_i) + Q_i \tag{27}$$

where ρ_i is the charge density, σ_i is the charge conductivity, Φ_i is the local electrostatic potential and Q_i is the charge source term.

Potential application between the anode and cathode electrodes in the solid oxide single pellet leads to transportation of charge throughout the pellet, and to exchanges of ionic to electronic charge and the vice versa, at the anodic and cathodic TPBs due to the electrochemical reactions taking place there (see Table III). Considering no charge source, the ionic and electronic charge conservation in the electrolyte and at the two electrodes

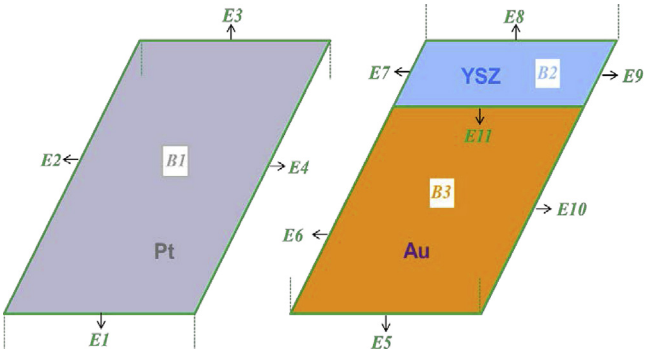

Fig. 4. The 3-D Computational domain numbering of boundaries and edges.

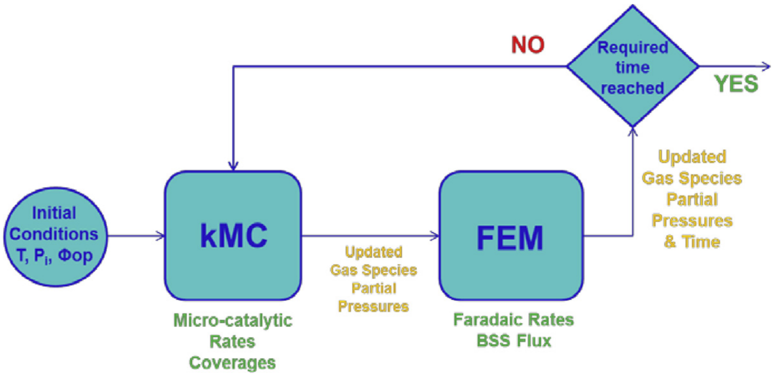

Fig. 5. Schematic of the multi-scale framework algorithm.

respectively, can be described as follows:

$$\frac{d\rho_{io}}{dt} = -\nabla\left(-\sigma_{io}\nabla\Phi_{io}\right) \tag{28}$$

$$\frac{d\rho_{el}^{A/C}}{dt} = -\nabla\left(-\sigma_{el}^{A/C}\nabla\Phi_{el}^{A/C}\right) \tag{29}$$

where ρ_{io} and $\rho_{el}^{A/C}$ are the ionic and electronic charge densities, σ_{io} and $\sigma_{el}^{A/C}$ are the ionic and electronic conductivities, and, Φ_{io} and $\Phi_{el}^{A/C}$ are the ionic and electronic potentials respectively. The superscripts A/C stand for the Anode/Cathode electrode domains.

The gaseous phase species' Faradaic rates and the BSS Faradaic generation rate due to the electrochemical reactions (7) to (10) occuring at the TPBs of the cathode and the anode are described by the following expressions:

$$\hat{R}_{CO_2}{}^{FEM} = \int_0^W\int_0^{L_a}\frac{I_8^A}{2F}\mathrm{dxdz} \tag{30}$$

$$\hat{R}_{CO}{}^{FEM} = -\int_0^W\int_0^{L_a}\frac{I_8^A}{2F}\mathrm{dxdz} \tag{31}$$

$$\hat{R}_{O_2}{}^{FEM} = \int_0^W\int_0^{L_a}\frac{I_9^A}{4F}\mathrm{dxdz} - \int_0^W\int_0^{\mathrm{L_C}}\frac{I^C}{2F}\mathrm{dxdz} \tag{32}$$

Table IV
Multi-scale framework utilised parameters.

Parameter	Symbol	Value
Pt specific site density, mol m^{-2}	$\mathrm{N_S}$	2.5407×10^{-5} [20]
Sticking coefficient of O_2 on Pt	S_{O_2}	7.69×10^{-5} [1]
Sticking coefficient of CO on Pt	$\mathrm{S_{CO}}$	5.38×10^{-1} [1]
O_2 desorption pre-exponential factor, s^{-1}	$k_{o,-1}^{d}$	2.4×10^{13} [15]
O_2 desorption activation energy, J mol^{-1}	$E_{A,-1}^{d}$	243139 [1]
CO desorption pre- exponential factor, s^{-1}	$k_{o,-2}^{d}$	6.5×10^{13} [15]
CO desorption activation energy, J mol^{-1}	$E_{A,-2}^{d}$	99618 [1]
CO and O_2 surface reaction pre-exp factor, s^{-1}	$k_{o,3}^{r}$	2.7×10^{6} [15]
CO oxidation activation energy, J mol^{-1}	$E_{A,3}^{r}$	35186 [1]
CO and BSS surface reaction rate constant, s^{-1}	k_4^r	5.73×10^{-3} [1]
BSS desorption rate constant, s^{-1}	k_5^d	4.27×10^{-3} [1]
BSS continuum diffusion coefficient, m^2 s^{-1}	$\mathrm{D_{BSS}}$	4×10^{-15} [34]
BSS diffusion rate constant (kMC), s^{-1}	k_{diff}^{BSS}	8.4×10^{-2} (using Eq.(23))
Cathodic charge transfer coefficient	α^{C}	0.5
Anodic charge transfer coefficient	α^{A}	0.5
Anode activation energy, J mol^{-1}	$\mathrm{E_A^A}$	120000 [1]
Cathode activation energy, J mol^{-1}	$\mathrm{E_A^C}$	110000 [1]
Cathode pre-exponential coefficient, A m^{-2}	γ_{C}	6.91×10^{8} [1]
Anode pre-exponential coefficient, A m^{-2}	$\gamma_{\mathrm{A,1}}$	5.01×10^{8} [1]
Anode pre-exponential coefficient, A m^{-2}	$\gamma_{\mathrm{A,2}}$	2.92×10^{11} [1]
Anode pre-exponential coefficient, A m^{-2}	$\gamma_{\mathrm{A,3}}$	3.42×10^{4} [1]
Anode (Pt) electrical conductivity, Ω^{-1} m^{-1}	σ_{el}^{A}	as in [16]
Cathode (Au) electrical conductivity, Ω^{-1} m^{-1}	σ_{el}^{C}	as in [16]
Electrolyte (YSZ) electrical conductivity, Ω^{-1} m^{-1}	σ_{io}	as in Eq. (53)
O_{YSZ}^{2-} chemical potential, J mol^{-1}	$\mu_{O_{YSZ}^{2-}}$	-236.4×10^{3} [35,36]
CO standard chemical potential, J mol^{-1}	μ_{CO}^{o}	-137.3×10^{3} [37]
CO_2 standard chemical potential, J mol^{-1}	$\mu_{CO_2}^{o}$	-394.4×10^{3} [37]

$$\hat{R}_{BSS}{}^{FEM} = \int_0^W \int_0^{L_a} \frac{I_{10}^A}{2F} \mathrm{d}x\mathrm{d}z \tag{33}$$

where W is the width of both anode and cathode electrodes, $L_{a/c}$ is the length of anode and cathode electrodes respectively, F is the Faraday constant, $I_i^{A/C}$ denotes the current density distribution of the Anode/Cathode computed by Eq.(43) and Eq.(37), respectively.

2.3.1. Boundary conditions

The numbering of boundaries (B) and edges (E) of the 3D computational domain is presented in Fig. 4. There are in total 7 boundaries and 15 edges, 6 of which, E2–4, E6 and E10–11 represent TPBs. It should be noted that boundaries B1 and B3 represent the anodic (Pt) and cathodic (Au) electrodes respectively.

For the solution of the set of PDEs that describe the charge transfer in the pellet, boundary conditions need to be imposed. The electronic potential is fixed to the value of the operating potential Φ_{op} at edge E5 and to 0 at E1.

$$\mathrm{E5}: \quad \Phi_{el}^C = \Phi_{op} \tag{34}$$

$$\mathrm{E1}: \quad \Phi_{el}^A = 0 \tag{35}$$

Transfer of electronic to ionic current occurs at the TPBs of the cathode that are represented by E6 and E10–11. Hence:

$$\mathrm{E6 \ \ and\, E10-11}: \quad \begin{aligned} -\mathrm{n}\cdot(-\sigma_{el}^C \nabla \Phi_{el}^C) &= I^C \\ -\mathrm{n}\cdot(-\sigma_{io} \nabla \Phi_{io}) &= -I^C \end{aligned} \tag{36}$$

where I^C is the current density distribution of the cathode which is due to the electrochemical reaction (7) taking place at the cathodic TPBs. The current density of the cathode can be expressed using the Butler-Volmer equation as:

$$I^C = 3 \times I_0^C \left[\exp\left(\alpha^c \frac{n_e F}{RT} \eta^c \right) - \exp\left(-(1-\alpha^c) \frac{n_e F}{RT} \eta^c \right) \right] \tag{37}$$

where I_0^C is the exchange current density of the cathode the expression of which can be found in Fragkopoulos et al. [1], n_e is the number of electrons transferred in the cathodic electrochemical reaction, α^C is the cathodic charge transfer coefficient and η^C is the overpotential of the cathode. The factor of 3 in the above expression is due to the parallel electrical circuit analogy [1,38].

The overpotential of the cathode is defined as [39]:

$$\eta^C = V_{OC} - \left(\Phi_{el}^C - \Phi_{io} \right) \tag{38}$$

where Φ_{el}^C and Φ_{io} are the local equilibrium potentials of the cathode and the electrolyte mediums respectively, and V_{OC} is the thermodynamic open circuit potential given by [1]:

$$V_{OC} = V_{OC}^o - \frac{1}{2F} \mu_{BSS}^A + \frac{RT}{2F} \ln\left(\frac{P_{CO}^A}{P_{CO_2}^A} \right) + \frac{RT}{2F} \ln\left(\frac{\left(P_{O_2}^C\right)^{3/2}}{\left(P_{O_2}^A\right)^{1/2}} \right) \tag{39}$$

where μ_{BSS}^A is the chemical potential of BSS, F is the Faraday constant, P_i is the partial pressure for species i in the gas phase (subscripts A and C stand for anode and cathode respectively) and V_{OC}^o is the *ideal Nernst potential* expressed as [1]:

$$V_{OC}^o = \frac{1}{2F} \left(\mu_{O_2}^o + \mu_{CO}^o - \mu_{CO_2}^o \right) \tag{40}$$

where μ_i^0 is the chemical potential of species i at standard conditions.

Ionic charge is transferred to electronic at edges E2–4 which represent the anodic TPBs. Hence:

$$\mathrm{E2-4} \quad \begin{aligned} -\mathrm{n}\cdot(-\sigma_{io} \nabla \Phi_{io}) &= I^A \\ -\mathrm{n}\cdot(-\sigma_{el}^A \nabla \Phi_{el}^A) &= -I^A \end{aligned} \tag{41}$$

where I^A is the total current density of the anode which is due to the electrochemical reactions (8) to (10) taking place at the anodic TPBs. The total current density of the anode can be expressed using the parallel electrical circuit analogy as [38]:

$$I^A = I_8^A + I_0^A + I_{10}^A \tag{42}$$

where I_8^A, I_9^A and I_{10}^A are the current density distributions due to the electrochemical reactions (8), (9) and (10), respectively, given by the following expression [40,41]:

$$I_i^A = I_{0,i}^A \left[\exp\left(\alpha^A \frac{n_e F}{RT} \eta^A \right) - \exp\left(-(1-\alpha^A) \frac{n_e F}{RT} \eta^A \right) \right], \quad i = 8, 9, 10 \tag{43}$$

where $I_{0,i}^A$ is the exchange current density of the anode for each electrochemical reaction i, the expression of which can be found in Fragkopoulos et al. [1], α^A is the anodic charge transfer coefficient and η^A the overpotential of the anode.

The overpotential of the anode is given by:

$$\eta^A = \Phi_{el}^A - \Phi_{io} \tag{44}$$

where Φ_{el}^A and Φ_{io} are the electronic and ionic potentials at the anode side respectively.

At all the remaining boundaries and edges the no flux condition is imposed for both ionic and electronic charge transfer.

2.4. The FEM/kMC multi-scale framework coupling

The macroscopic and microscopic simulators are communicating their respective outputs through the update of the partial pressures of the gaseous phase species and also through the BSS (generated during the macroscopic simulation) feed in the kMC simulation.

The partial pressures of the gaseous species are updated using the following expressions:

$$P_{CO_2}^{new} = \frac{RT}{F_d} \left(\hat{R}_{CO_2}{}^{FEM} + \hat{R}_{CO_2}{}^{KMC} \right) \tag{45}$$

$$P_{CO}^{new} = P_{CO}^{in} + \frac{RT}{F_d} \left(\hat{R}_{CO}{}^{FEM} + \hat{R}_{CO}{}^{KMC} \right) \tag{46}$$

$$P_{O_2}^{new} = P_{O_2}^{in} + \frac{RT}{F_d} \left(\hat{R}_{O_2}{}^{FEM} + \hat{R}_{O_2}{}^{KMC} \right) \tag{47}$$

$$P_{He}^{new} = P_T - \left(P_{O_2}^{new} + P_{CO}^{new} + P_{CO_2}^{new} \right) \tag{48}$$

where P_i^{new} is the updated partial pressure of species i, P_i^{in} is the partial pressure of species i at the inlet of the reactor, F_d is the volumetric flowrate of the gas mixture, R is the ideal gas constant, $\hat{R}_i{}^{FEM}$ and $\hat{R}_i{}^{FEM}$ the Faradaic (computed through macroscopic FEM simulations) and catalytic rates (computed through kMC simulations) (in mol/s units) given by Eq.(30) to Eq.(32) and Eq. (26), respectively.

The macroscopic generation of oxygen BSS ($[O^{2-}$- $\delta^{2+}]$), using a similar correlation to the one presented in Karavasilis et al. [42] for sodium backspillover species ($[Na^{+}$ - $\delta^{-}]$), is given by:

$$\frac{d\theta_{BSS}}{dt} = \frac{\hat{R}_{BSS}^{FEM}}{N_S A_S} \quad (49)$$

where $\hat{R}_{BSS}^{FEM}$ is the Faradaic generation of BSS (Eq.(33)), N_S is the catalyst site density and A_S is the catalytic surface area.

Eq.(49), taking into account the number of lattice sites occupied by BSS, Ω_{BSS^*}, and that $\theta_{BSS} = \Omega_{BSS^*}/\Omega_T$ and $A_S = \Omega_T/N_S N_{AV}$, takes the form:

$$\frac{d\Omega_{BSS^*}}{dt} = \hat{R}_{BSS}^{FEM} N_{AV} \quad (50)$$

and subsequently (for relatively small reporting horizons, t_{rep}^{kMC}):

$$\frac{\Omega_{BSS^*}\left(t + t_{rep}^{kMC}\right) - \Omega_{BSS^*}(t)}{t_{rep}^{kMC}} = \hat{R}_{BSS}^{FEM} N_{AV} \quad (51)$$

where N_{AV} is the Avogadro number, $\Omega_{BSS^*}\left(t + t_{rep}^{kMC}\right)$ is the number of BSS molecules at the end of the time reporting horizon and $\Omega_{BSS^*}(t)$ is the number of BSS molecules at the beginning of the time reporting horizon.

Thus, the total number of BSS molecules, n_{BSS}, to be introduced into the kMC simulator during each reporting horizon, taking into consideration that $n_{BSS} = \Omega_{BSS^*}\left(t + t_{rep}^{kMC}\right) - \Omega_{BSS^*}(t)$, is given by:

$$n_{BSS} = \hat{R}_{BSS}^{FEM} N_{AV} t_{rep}^{kMC} \quad (52)$$

While n_{BSS} is a continuous variable, only the integer part of it is taken into account to calculate the number of BSS molecules introduced into the lattice.

Szymczak and Ladd [43] suggest that in a continuous process, it is not enough to just introduce the correct number of molecules in a domain but also the technique for this introduction is important. They found that is more accurate to release the molecules continuously over a time horizon rather than at the beginning of it. Taking this into consideration, the molecules (calculated using Eq. (52)) are introduced into the lattice using a timestep randomly chosen from a uniform distribution in the range [t, t+ t_{rep}^{kMC}] and are being randomly placed at empty sites available at the lattice boundaries.

A schematic representation of the multi-scale framework algorithm is illustrated in Fig. 5. Initial conditions for temperature, T, gaseous species' partial pressures, P_i, and operating potential, Φ_{op}, are fed into the microscopic simulator $\hat{R}_i^{FEM} = 0$and at the end of a time reporting horizon (chosen here as t_{rep}^{kMC} =10^{-5}s), the lattice kMC simulator provides the production/consumption rates of each gaseous species, $\hat{R}_i^{kMC}$, computed by Eq.(26). The partial pressures of the gaseous species are then updated using Eq.(45) to Eq.(48) taking into account the c ($\hat{R}_i^{KMC}$). It is worthwhile to note here that for the first update of the partial pressures, the Faradaic rates computed by Eq.(30) to Eq.(32) are not taken into account ($\hat{R}_i^{FEM} = 0$, since the macroscopic run has not yet been performed). The computed partial pressures are subsequently fed into the macroscopic simulator and at the end of the same time reporting horizon, the model provides the Faradaic rates for each species (Eq. (30) to Eq.(32)) and a Faradaic generation term for BSS (Eq.(33)). The partial pressures of the gaseous species are updated again, now taking into account the values of the current $\hat{R}_i^{FEM}$ and of the previously calculated $\hat{R}_i^{kMC}$, and are fed back to the microscopic simulator also providing the calculated number of BSS (Eq. (52)). This process is continued until the total desired time is reached.

3. Numerical solution approach

COMSOL Multiphysics is utilised as the partial differential equation solver where the FEM is employed for the simultaneous solution of the set of PDEs described by equations (28) and (29) at the macroscopic level. The 3-D computational domain is discretised in 38,876 tetrahedral triangular elements and the GMRES system solver (Incomplete LU preconditioner, 0.01 drop tolerance) in COMSOL is chosen for the solution of the set of equations. The charge conservation in the anode and cathode electrodes is implemented using the weak form boundary PDEs incorporated in COMSOL. The kinetic Monte Carlo method is employed for the simulation of the reaction-diffusion micro-processes (as in Table I) taking place on the catalytic surface. The 2D catalytic surface is represented by a 1800 × 400 sites micro-lattice (respective to the L_axW (460 nm by 102.3 nm, see Table I) macro-lattice using the selected site density, N_S). Such a small catalytic surface was chosen in this work for two reasons: (i) The simulation of the multi-scale system can be performed with efficiency at relatively short times and with small memory requirements and (ii) it represents an actual nano-patterned experimental system currently being set up by a collaborating experimental group [44]. The macro- and microscopic models interact at the anodic triple phase boundaries via the BSS Faradaic generation (Eq.(33)) and also through the gaseous species partial pressures updates (Eq.(45) to (48)). MATLAB R2012b [45] is used as the interface between the macro- and micro-scopic models the codes of which are written in COMSOL scripts and in standard FORTRAN 90 [46], respectively.

The selected framework parameters are tabulated in Table IV along with their corresponding sources. The electronic charge conductivities, σ_{el}^{A} and σ_{el}^{C}, can be found in COMSOL Material Library [16], while the ionic charge conductivity is given by [47]:

$$\sigma_{io}^{YSZ} = 33.4 \cdot 10^{3} \exp\left(\frac{-10300}{T}\right) \quad (53)$$

Table V
Multi-scale framework operating conditions.

Parameter	Symbol	Value
Operating (reference) pressure, atm	P_T	1
Faraday's constant, A s mol^{-1}	F	96485
Volumetric flowrate of gas mixture, $m^3 s^{-1}$	F_d	2.5×10^{-6}
Operating potential, mV	Φ_{op}	700

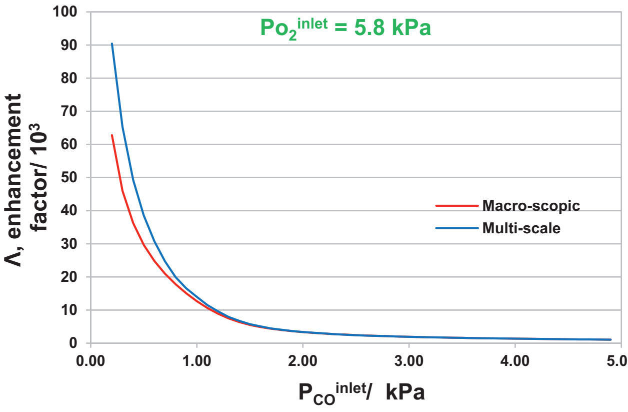

Fig. 6. Effect of inlet partial pressure of CO on enhancement factor Λ.

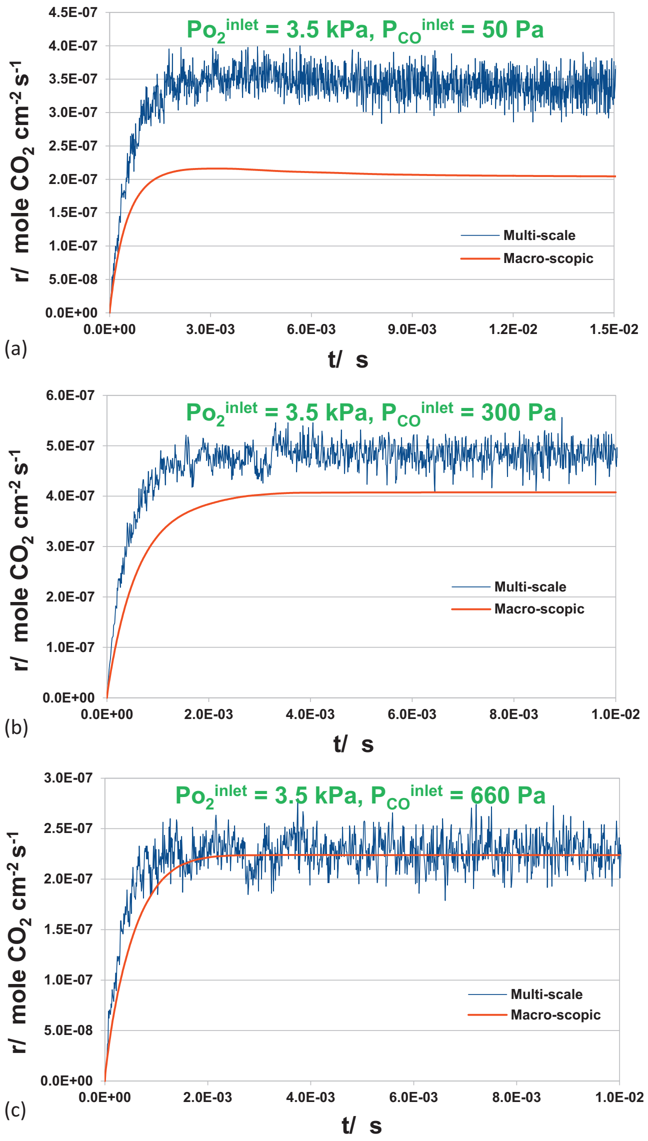

Fig. 7. Transients of CO_2 production normalised rate, at T = 350 °C, for an inlet partial pressure of O_2,$P^{in}_{O_2}$ = 3.5 kPa, and an inlet partial pressure of CO: (a) P^{in}_{CO} = 50 Pa, (b) P^{in}_{CO} = 300 Pa, (c) P^{in}_{CO} = 660 Pa.

4. Results and discussion

The operating conditions utilised in the multi-scale framework are listed in Table V. The operating potential, Φ_{op}, is fixed to 700 mV and is considered to be constant throughout the solid oxide single pellet. Also, the pellet is assumed to be preheated at the system operating temperature. The non-Faradaic efficiency of the multi-scale system is depicted in Fig. 6. The effect of the inlet CO partial pressure on the enhancement factor, Λ, computed by the multi-scale framework, follows the same trend with the one calculated by a macroscopic model we have previously developed [1], while the values of Λ of the order of 10^3 demonstrate how strong the non-Faradaic effect is for this system. Also, as it can be seen in Fig. 6 the multi-scale models predicts higher Λ, at low CO inlet partial pressures below 1 kPa at the selected operating conditions.

Comparisons between the CO_2 production rate dynamic profiles multi-scale framework and our previously developed macroscopic model of the same system [1] are carried out under atmospheric conditions, through investigating the transient and the steady state behaviours resulting from each modelling study. Furthermore, the multi-scale framework is exploited for the investigation of the effect of the gaseous species partial pressures and of the operating temperature on the CO_2 production rate.

4.1. Transient results

Comparisons between the CO_2 production rate dynamic profiles resulting from the macroscopic and the multi-scale frameworks at a temperature T = 623.15 K, for an inlet partial pressure of O_2, $P^{in}_{O_2} = 3.5$kPa, and for different CO partial pressures are depicted in Fig. 7a–c. We can observe that although the dynamics of the models are similar, quantitative differences are exhibited in their steady state responses. More specifically, the multi-scale framework predicts greater CO_2 production rates, with a relative difference of about 70%, than the CO_2 production rates predicted by the macroscopic model for the combination of $P^{in}_{O_2} = 3.5$kPa and

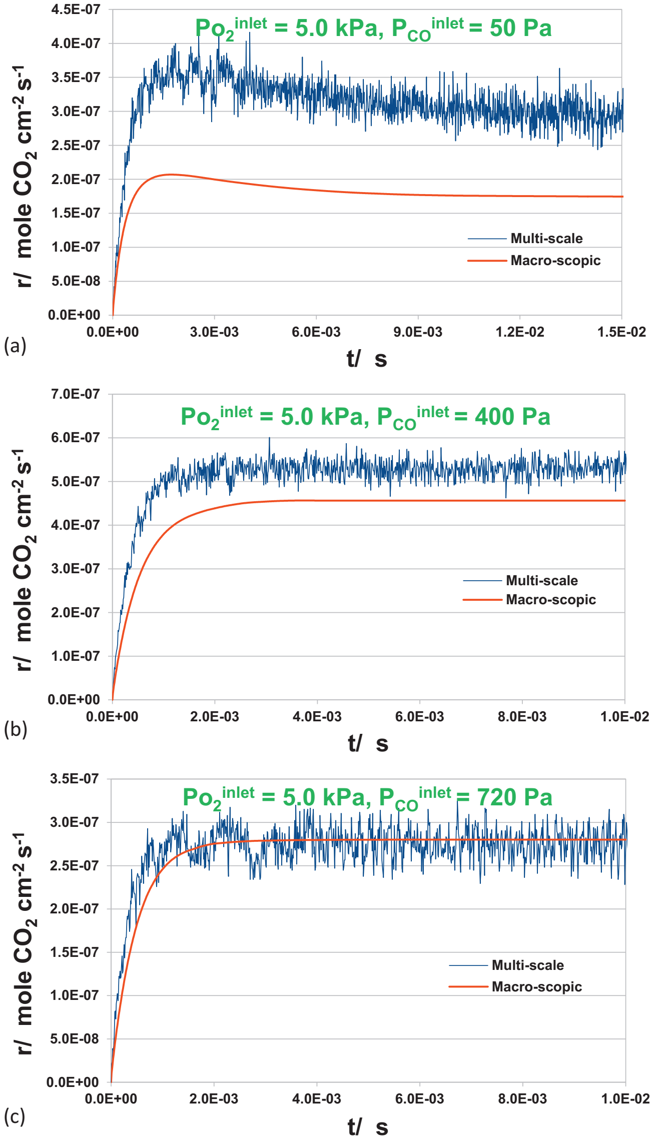

Fig. 8. Transients of CO_2 production normalised rate, at T = 350 °C, for an inlet partial pressure of O_2, $P^{in}_{O_2}$ = 5.0 kPa, and an inlet partial pressure of CO: (a) P^{in}_{CO} = 50 Pa, (b) P^{in}_{CO} = 400 Pa, (c) P^{in}_{CO} = 720 Pa.

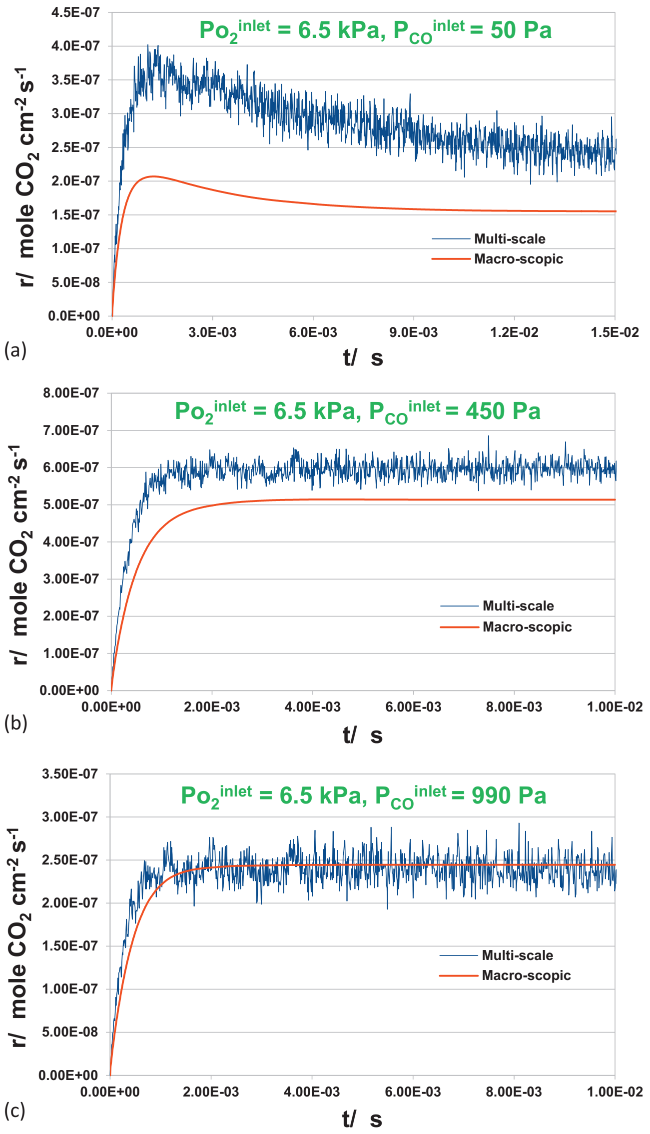

Fig. 9. Transients of CO_2 production normalised rate, at T = 350 °C, for an inlet partial pressure of O_2, $P_{O_2}^{in} = 6.5$ kPa, and an inlet partial pressure of CO: (a) $P_{CO}^{in} = 50$ Pa, (b) $P_{CO}^{in} = 450$ Pa, (c) $P_{CO}^{in} = 990$ Pa.

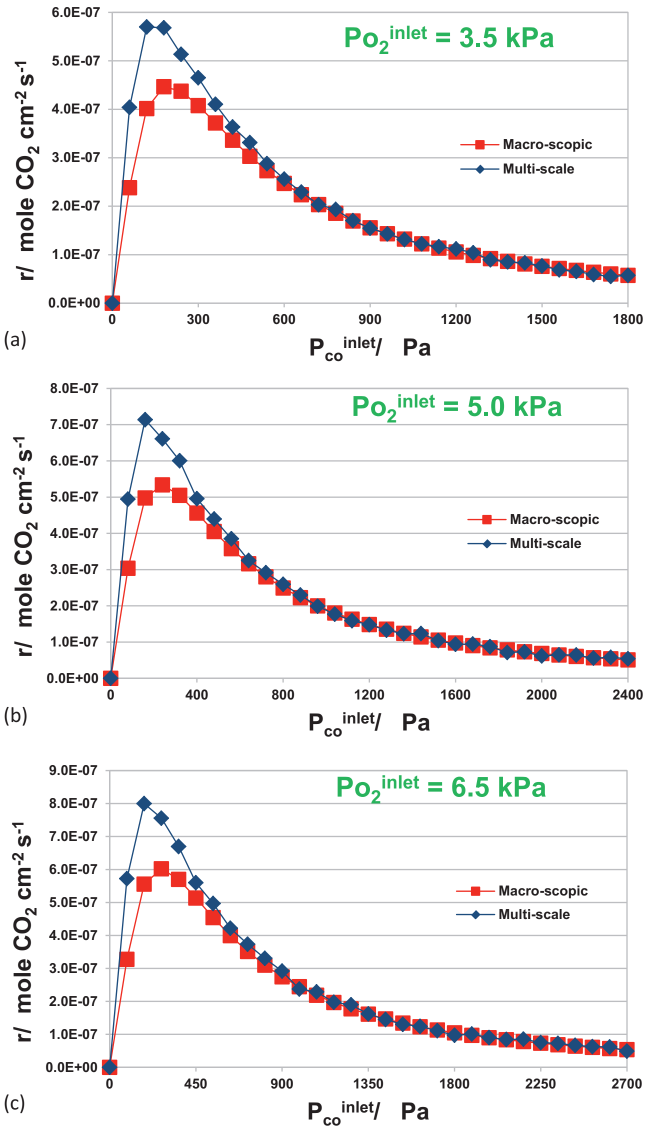

Fig. 10. Steady state effect of inlet partial pressure of CO on CO_2 production normalised rate, at T = 350 °C and for an inlet partial pressure of O_2: (a) $P_{O_2}^{in} = 3.5$ kPa, (b) $P_{O_2}^{in} = 5.0$ kPa, (c) $P_{O_2}^{in} = 6.5$ kPa.

$P_{CO}^{in} = 50$Pa operating partial pressures (Fig. 7a). Increasing the CO partial pressure to $P_{CO}^{in} = 300$Pa (Fig. 7b) leads to a decreased relative difference of 20% and in the case of $P_{CO}^{in} = 660$Pa (Fig. 7c) we have almost identical responses. Hence, the macroscopic model predicts lower CO_2 production rates than the ones predicted by the multi-scale model for low CO partial pressures, while the systems tend to the same quantitative behaviour for larger CO partial pressures. Fig. 7a–c shows that the macroscopic model simulation can accurately replace the multi-scale system one for high CO partial pressures, while multi-scale simulations are necessary for accurate CO_2 production rate estimations at low CO partial pressures. This is expected, since high CO partial pressures result in CO high coverages and to subsequent reduced interactions with adsorbed O molecules.

The CO_2 production rate transients were further investigated using different sets of operating conditions. Figs. 8a–c and 9a–c illustrate the CO_2 production rate differences between the two modelling frameworks for $P_{O_2}^{in} = 5.0$kPa and $P_{O_2}^{in} = 6.5$kPa respectively. The dynamic trends of the models are again here similar. Decreasing differences are observed between the models ' steady state outputs when P_{CO}^{in} was increased. Moreover, as we can observe in Figs. 7a–c, 8a–c and 9a–c, both modelling frameworks reach steady state at the same time for all utilised operating conditions, as expected due to the low BSS diffusion probability compared with the adsorption/desorption ones (same as in Raimondeau and Vlachos [25] for low CO diffusion probability).

4.2. Steady state results

The steady state effects (computed through dynamic simulations over sufficiently long times) of inlet partial pressure of CO on CO_2 production rate for both macroscopic and multi-scale models, at a temperature T = 623.15 K and for inlet partial pressures of O_2, $P_{O_2}^{in} = 3.5$kPa, 5kPa and 6.5kPa are summarised in Fig. 10a–c respectively.

A typical "volcano-type" behaviour [5] is observed in the CO_2 production rate for both frameworks. Greater differences are

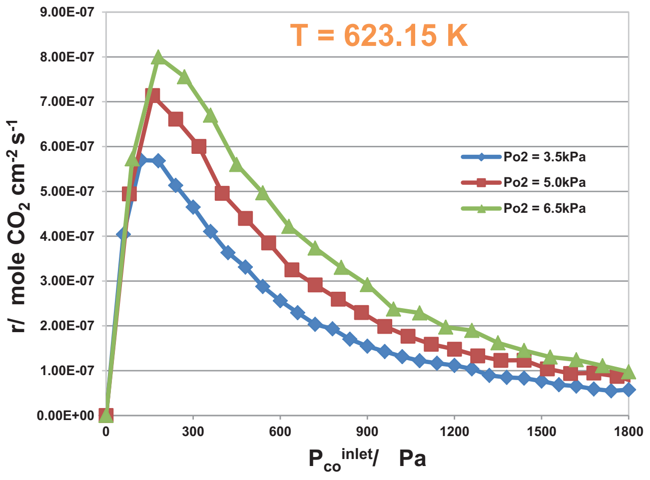

Fig. 11. Steady state effect of inlet partial pressure of O_2 on CO_2 production normalised rate, for an increasing inlet partial pressure of CO and at T = 350 °C.

observed between the models' corresponding outputs for relatively low CO inlet partial pressures.

The produced CO_2 reaches a maximum value at $P^{in}_{O_2}/P^{in}_{CO} \approx 30$ as computed by the multi-scale framework and at $P^{in}_{O_2}/P^{in}_{CO} \approx 20$ as computed by the macroscopic model. Moreover, the macroscopic model predicts a lower maximum CO_2 production rate than the multi-scale one, illustrating the importance of accurate simulations in such a system where maximum CO_2 production rate is desired.

For $P^{in}_{O_2}/P^{in}_{CO} < 30$, the differences between the models' steady state outputs are getting reduced when increasing the CO inlet partial pressure and for $P^{in}_{O_2}/P^{in}_{CO} < 7$ minor or no differences are observed. Reducing discrepancies between the mean field and the kMC rates for increasing CO partial pressures has been reported in the literature [25]. Raising the CO partial pressures leads to increasing CO adsorption rates and to subsequent CO higher coverages. The higher the CO coverage the lower the interactions between adsorbed CO and O surface species.

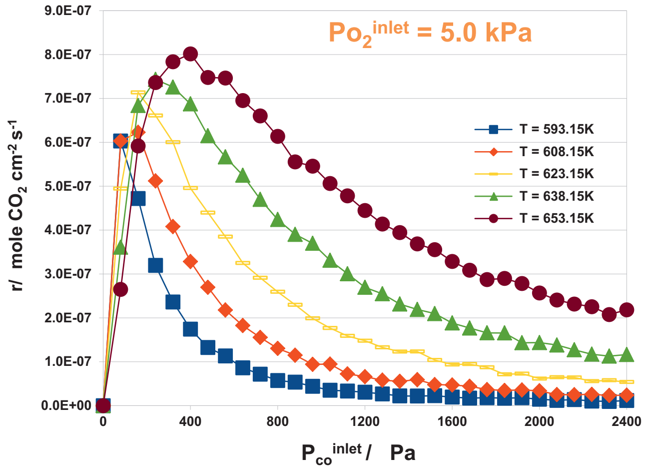

Fig. 12. Steady state effect of temperature on CO_2 production normalised rate, for a set inlet partial pressure of O_2 and an increasing inlet partial pressure of CO (T = 320–380 °C).

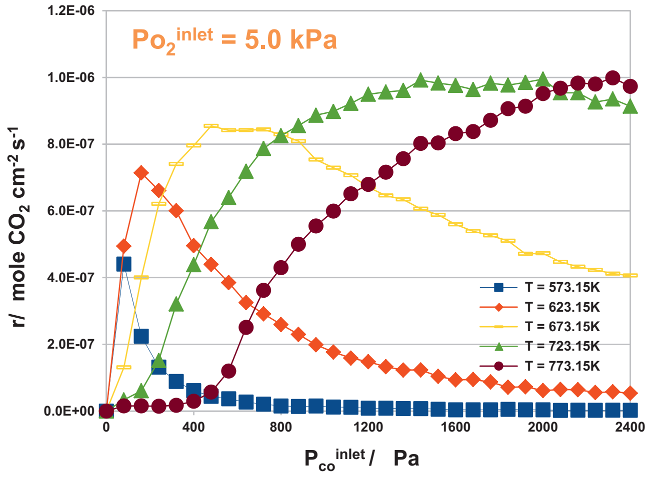

Fig. 13. Steady state effect of temperature on CO_2 production normalised rate, for a set inlet partial pressure of O_2 and an increasing inlet partial pressure of CO (T = 300–500 °C).

4.3. Parametric study

Parametric studies have also been performed, using the multi-scale framework, in order to investigate the effect of operating conditions on CO_2 production rate.

Effect of $P^{in}_{O_2}$. The effect of $P^{in}_{O_2}$ on CO_2 production rate at a temperature T = 623.15 K and for increasing P^{in}_{CO} values is illustrated in Fig. 11. A "volcano-type" behaviour is found in the CO_2 production rate. We can also observe that increasing the O_2 inlet partial pressure leads to greater CO_2 production rates and subsequently to better catalytic performance.

Effect of Temperature. The effect of temperature on CO_2 production rate for $P^{in}_{O_2} = 5$kPa and for temperatures between 320 °C and 380 °C is depicted in Fig. 12. As we can see, small increases in the system operating temperature lead to noticeable increases in the electrochemically promoted CO_2 production rate as expected, since the surface reaction probability increases with increasing operating temperature. Increasing the system operating temperature leads to a consequent increase in the CO desorption probability which as a result shifts the maximum production of CO_2 towards slightly greater P^{in}_{CO} values.

The effect of the system operating temperature on the electrochemically promoted CO_2 production rate is further investigated for temperature ranges between 300 °C and 500 °C (as the NEMCA effect in such systems is observed in that range of temperature values [48–50]) and presented in Fig. 13. As we can observe, temperature increases lead to significant increases of the catalytic performance. Also, "volcano-type" behaviour is observed for temperatures lower or equal to 400 °C, while "S-type" behaviour is favoured for temperatures greater or equal to 450 °C.

5. Conclusions

The objective of this study was the formulation of a 3-dimensional, isothermal, dynamic solid oxide single pellet multi-scale framework to describe the chemical and electrochemical processes taking place in the system under application of potential. The proposed framework is integrated by a 3-D macroscopic model which simulates the charge transport throughout the pellet as well as the electrochemical processes taking place at the triple phase boundaries of the anode and the cathode, and a 2-D microscopic model which simulates the reaction-diffusion micro-processes taking place on the catalytic surface of the anode. COMSOL Multiphysics is utilised for the simultaneous simulation of the set of charge conservation PDEs employing the finite element method, while an in-house developed lattice kMC model is employed to perform the microscopic simulation. The proposed framework allows the prediction of electronic and ionic potential curves, species coverage on the catalytic micro-lattice, transients of gas mixture concentration in the reactor, and it also provides CO_2 Faradaic and non-Faradaic production rates.

CO_2 production rate curves have been computed to compare the performance of the proposed multi-scale framework with that predicted by a macroscopic model under atmospheric conditions. The models were found to exhibit similar dynamic trends for the sets of utilised conditions. However, quantitative differences have been observed between their steady state CO_2 production rates. The predicted CO_2 production rates (in $\text{mol cm}^{-2}\,\text{s}^{-1}$) are found to be of the order of 10^{-7} which is quite reasonable for such systems [5]. Rising CO inlet partial pressures is leading to reducing differences between the models' steady state predictions and also to minor or almost no differences for $P^{in}_{O_2}/P^{in}_{CO} < 7$. Moreover, the maximum catalytic performance is predicted at $P^{in}_{O_2}/P^{in}_{CO} \approx 30$ by the multi-scale framework and at $P^{in}_{O_2}/P^{in}_{CO} \approx 20$ by the macroscopic model. These observations suggest that the macroscopic model simulation can accurately replace the multi-scale system one for high CO partial pressures, while the use of the multi-scale system is beneficial for accurate maximum CO_2 production rate estimations at low CO partial pressures.

The multi-scale framework was further exploited for temperature parametric studies. We have observed that temperature increases result in significant increases of the CO_2 production rate through increasing the surface reaction probability. Also, alterations in the system's behaviour have been observed. “Volcano-type” behaviour was favoured for temperatures lower or equal to 400 °C and “S-type” behaviour was observed for temperatures greater or equal to 450 °C.

Acknowledgements

Financial support (Grant EP/G022933/1) from the Engineering and Physical Sciences Research Council (EPSRC) is gratefully acknowledged. ISF also wishes to acknowledge the EPSRC support through his doctoral prize fellowship 2013/2014.

References

[1] I.S. Fragkopoulos, I. Bonis, C. Theodoropoulos, Macroscopic multi-dimensional modelling of electrochemically promoted systems, Chemical Engineering Science 104 (2013) 647–661.
[2] J. Pritchard, Electrochemical Promotion, Nature 343 (1990) 592–593.
[3] M. Stoukides, C.G. Vayenas, The effect of electrochemical oxygen pumping on the rate and selectivity of ethylene oxidation on polycrystalline silver, Journal of Catalysis 70 (1981) 137–146.
[4] A. Katsaounis, Electrochemical promotion of catalysis (EPOC) perspectives for application to gas emissions treatment, Global NEST Journal 10 (2008) 226–236.
[5] C.G. Vayenas, S. Bebelis, C. Pliangos, S. Brosda, D. Tsiplakides, Electrochemical activation of catalysis: Promotion, electrochemical promotion, and metal-support interactions, Kluwer Academic/Plenum Publishers, New York, 2001.
[6] E. Weinan, Principles of multiscale modeling, Cambridge University Press, 2011.
[7] M. Andersson, B. Yuan, Sundén, Review on modeling development for multiscale chemical reactions coupled transport phenomena in solid oxide fuel cells, Applied Energy 87 (2010) 1461–1476.
[8] G.D. Ingram, I.T. Cameron, K.M. Hangos, Classification and analysis of integrating frameworks in multiscale modelling, Chemical Engineering Science 59 (2004) 2171–2187.
[9] D. Maroudas, Multiscale modeling of hard materials: Challenges and opportunities for chemical engineering, AIChE Journal 46 (2000) 878–882.
[10] C. Pantelides, New challenges and opportunities for process modelling, Computer Aided Process Engineering 11 (2001) 15–26.
[11] W.G. Bessler, S. Gewies, S. Vogler, A new framework for physically based modeling of solid oxide fuel cells, Electrochimica Acta 53 (2007) 1782–1800.
[12] M.A. Khaleel, D.R. Rector, Z. Lin, K. Johnson, K. Rechnagle, Multiscale electrochemistry modeling of solid oxide fuel cells, International Journal for Multiscale Computational Engineering 3 (2005) 33–48.
[13] J.H. Kim, W.K. Liu, C. Lee, Multi-scale solid oxide fuel cell materials modeling, Computational Mechanics 44 (2009) 683–703.
[14] S.F. Lee, C.W. Hong, Multi-scale design simulation of a novel intermediate-temperature micro solid oxide fuel cell stack system, International Journal of Hydrogen Energy 35 (2010) 1330–1338.
[15] D.J. Kaul, R. Sant, E.E. Wicke, Integrated kinetic modeling and transient FTIR studies of CO oxidation on Pt/SiO_2, Chemical Engineering Science 42 (1987) 1399–1411.
[16] COMSOL, COMSOL Multiphysics 4.2a - Reference Guide, COMSOL AB, 2011.
[17] I.S. Fragkopoulos, C. Theodoropoulos, Multiscale models of electrochemically-promoted large catalytic surfaces, Proceedings of the 3rd International Conference on Simulation and Modeling Methodologies, Technologies and Applications, SCITEPRESS (2013) 155–162.
[18] I.S. Fragkopoulos, I. Bonis, C. Theodoropoulos, Multiscale modelling of spillover processes in heterogeneous catalytic systems, Computer Aided Process Engineering 30 (2012) 1013–1017.
[19] B. Hari, C. Theodoropoulos, Integrated multi-scale models for simulation and design of microreactor systems, Chemical Engineering Transactions 17 (2009) 1269–1274.
[20] I.V. Yentekakis, G. Moggridge, C.G. Vayenas, R.M. Lambert, In situ controlled promotion of catalyst surfaces via NEMCA: The effect of Na on Pt-catalyzed CO oxidation, Journal of Catalysis 146 (1994) 292–305.
[21] D.T. Gillespie, A general method for numerically simulating the stochastic time evolution of coupled chemical, Journal of Computational Physics 22 (1976) 403–434.
[22] D.T. Gillespie, Exact stochastic simulation of coupled chemical reactions, The Journal of Physical Chemistry 81 (1977) 1340–1361.
[23] N. Metropolis, S. Ulam, The Monte Carlo method, Journal of the American Statistical Association 44 (1949) 335–341.
[24] J.S. Reese, S. Raimondeau, D.G. Vlachos, Monte Carlo algorithms for complex surface reaction mechanisms: Efficiency and accuracy, Journal of Computational Physics 173 (2001) 302–321.
[25] S. Raimondeau, D.G. Vlachos, The role of adsordate-layer nonuniformities in catalytic reactor design: Multiscale simulations for CO oxidation on Pt, Computers and Chemical Engineering 26 (2002) 965–980.
[26] D.J. Dooling, L.J. Broadbelt, Generic monte carlo tool for kinetic modeling, Industrial and Engineering Chemistry Research 40 (2001) 522–529.
[27] V.P. Zhdanov, B. Kasemo, Kinetic oscillations on nm-sized catalyst particles: Oxide model, Surface Science 511 (2002) 23–33.
[28] V.P. Zhdanov, B. Kasemo, Simulation of kinetic oscillations in the CO+O_2/Pt reaction on the nm scale, Journal of Catalysis 214 (2003) 121–129.
[29] K.A. Fichthorn, W.H. Weinberg, Theoretical foundations of dynamical Monte Carlo simulations, Journal of Chemical Physics 95 (1991) 1090–1096.
[30] S. Guerrero, E.E. Wolf, Kinetic Monte Carlo simulation of the preferential oxidation of CO using normally distributed rate probabilities, Chemical Engineering Science 66 (2011) 4477–4487.
[31] R. Phillips, Crystals, defects and microstructures: Modeling across the scales, Cambridge University Press, 1998.
[32] W.A. Tello, J.S. Curtin, A coupled discrete/continuum model for multiscale diffusion, International Journal for Multiscale Computational Engineering 3 (2005) 257–265.
[33] K. Tseronis, I. Bonis, I.K. Kookos, I.K. Theodoropoulos, Parametric and transient analysis of non-isothermal, planar solid oxide fuel cells, International Journal of Hydrogen Energy 37 (2011) 530–547.
[34] C.G. Vayenas, G.E. Pitselis, Mathematical modeling of electrochemical promotion and of metal-support interactions, Industrial and Engineering Chemistry Research 40 (2001) 4209–4215.
[35] W.G. Bessler, J. Warnatz, W.G. Goodwin, The influence of equilibrium potential on the hydrogen oxidation kinetics of SOFC anodes, Solid State Ionics 177 (2007) 3371–3383.
[36] M. Vogler, A. Bieberle-Hutter, L. Gauckler, J. Warnatz, W.G. Bessler, Modeling study of surface reactions, diffusion, and spillover at a Ni/YSZ patterned anode, Journal of the Electrochemical Society 156 (2009) B663–B672.
[37] J.H. Perry, R.H. Perry, C.H. Chilton, S.D. Kirkpatrick, Chemical Engineers' Handbook, 4th ed, John Wiley & Sons Inc., New York, 1963.
[38] E. Achenbach, Three-dimensional and time-dependent simulation of a planar solid oxide fuel cell stack, Journal of Power Sources 49 (1994) 333–348.
[39] R. Bove, S. Ubertini, Modeling solid oxide fuel cell operation: Approaches, techniques and results, Journal of Power Sources 159 (2006) 543–559.
[40] P. Aguiar, N.P. Adjiman, Brandon, Anode-supported intermediate temperature direct internal reforming solid oxide fuel cell: I: Model-based steady-state performance, Journal of Power Sources 138 (2004) 120–136.
[41] K. Tseronis, I.K. Kookos, C. Theodoropoulos, Modelling mass transport in solid oxide fuel cell anodes: A case for a multidimensional dusty gas-based model, Chemical Engineering Science 63 (2008) 5626–5638.
[42] C. Karavasilis, S. Bebelis, C.G. Vayenas, In Situ controlled promotion of catalyst surfaces via NEMCA: The effect of Na on the Ag-catalyzed ethylene epoxidation

in the presence of chlorine moderators, Journal of Catalysis 160 (1996) 205–213.

[43] P. Szymczak, A.J.C. Ladd, Stochastic boundary conditions to the convection-diffusion equation including chemical reactions at solid surfaces, Physical Review E 69 (2004) 36,704–1-9.

[44] I.S. Metcalfe, E. Papaioannou, Private Communication December 2013 (2013) .

[45] MATLAB, MATLAB® & SIMULINK® Release notes for Rb, 2012, The MathWorks, Inc., 2012.

[46] T.M.R. Ellis, I.R. Philips, T.M. Lahey, Fortran 90 programming, Addison-Wesley Publishers Ltd, Edinburgh Gate, 1994.

[47] J.R. Ferguson, J.M. Fiard, R. Herbin, Three-dimensional numerical simulation for various geometries of solid oxide fuel cells, Journal of Power Sources 58 (1996) 109–122.

[48] C.G. Vayenas, S. Bebelis, S. Neophytides, I.V. Yentekakis, Non-Faradaic electrochemical modification of catalytic activity in solid electrolyte cells, Applied Physics A: Materials Science and Processing 49 (1989) 95–103.

[49] C.G. Vayenas, S. Bebelis, Electrochemical promotion of heterogeneous catalysis, Catalysis Today 51 (1999) 581–594.

[50] C.G. Yentekakis, C.G. Vayenas, The effect of electrochemical oxygen pumping on the steady-state and oscillatory behavior of CO oxidation on polycrystalline Pt, Journal of Catalysis 111 (1988) 170–188.